Pre-Smectic Ordering and the Unwinding Helix in Monte Carlo Simulations of Cholesteric Liquid-Crystals

Paul Brumby, Akie Kowaguchi, Takuma Nozawa, Kenji Yasuoka, Henricus Herman Wensink

Pre-smectic ordering and the unwinding helix in Monte Carlo simulations of cholesteric liquid-crystals

Paul E. Brumby,*,† Akie Kowaguchi,† Takuma Nozawa,† Kenji Yasuoka,† and Henricus H. Wensink‡

†*Department of Mechanical Engineering, Keio University, 3-14-1 Hiyoshi, Kohoku-ku, Yokohama, 223-8522, Japan*

‡*Laboratoire de Physique des Solides - UMR 8502, Université Paris-Saclay & CNRS, 91405 Orsay, France*

E-mail: *p.brumby@keio.jp

Abstract

In this paper, molecular chirality is studied for liquid-crystal fluids represented by hard rods with the addition of an attractive chiral dispersion term. Chiral forces between molecular pairs are assumed to be long-ranged and are described in terms of the pseudotensor of Goossens [W. J. A. Goossens, Mol. Cryst. Liq. Cryst. **12**, 237–244 (1971)]. Following Varga and Jackson [S. Varga and G. Jackson, Chem. Phys. Lett. **377**, 6–12 (2003)], this is combined with a hard-spherocylinder core. We investigate the relationship between molecular chirality and the helical pitch of the system, which occurs in the absence of full three-dimensional periodic boundary conditions. The dependence of the wavenumber of this pitch on the thermodynamic variables, temperature, and density, is measured. We also explore the use of a novel surface boundary interaction model. As a result of this approach, we are able to lower the temperature of the system without the occurrence of nematic droplets, which would interfere with the formation of a uniaxial pitch. Regarding the theoretical predictions of Wensink and Jackson [H. H. Wensink and G. Jackson, J. Chem. Phys. **130**, 234911 (2009)], on the one hand, we have qualitative agreement with the observed non-monotonic density dependence of the wavenumber. Initially increasing with density, the wavenumber reaches a maximum, before falling as the density moves towards the point of phase transition from cholesteric to smectic. However, further analysis for shorter rods, in the presence of novel boundary conditions, reveals some disagreement with the theory, at least in this case; the unwinding of the cholesteric helix in the cholesteric phase occurs simultaneously with subtle increases in smectic ordering. These pre-smectic fluctuations have not been accounted for so far in theories on cholesterics but turn out to play a key role in controlling the pitch of cholesteric phases of rod-shaped mesogens with a small to moderate aspect ratio.

1 Introduction

Chirality is a fascinating property of certain objects that lack mirror symmetry. It is also a characteristic of a variety of molecule types.[1] When molecules or colloids are themselves chiral objects it is possible for them to form chiral liquid crystal phases, under certain conditions. The cholesteric phase shares many of the properties of its achiral counterpart, with molecules being positioned without order while

having orientational order along the nematic ordering director, $\hat{\mathbf{n}}$. In the cholesteric phase, this director gradually rotates along a particular axis, usually called the helical axis. The pitch, P, is the distance along the axis of rotation required to observe a 360° helical rotation of the nematic ordering director.

Molecular chirality is responsible for some of the most beautiful colours found in the natural world. For example, the iridescent metallic textures of specific types of beetle were found to be attributable to chiral structures covering their exoskeletons.[2] Chirality is also a vital property of life itself,[3] with cholesteric phases being formed by various types of biological helices,[4] including DNA.[5,6] However, the precise microscopic origins of chirality remain unclear. Experimental studies on suspensions of rod-like viruses have revealed the macroscopic pitch to have complicated relationships with microscopic properties, such as handedness,[7] helicity[8] and contour length,[9,10] as well as other factors such as the suspending fluid's ionic strength.[11,12] Likewise, experiments with various other cholesteric phases suggest a clear decrease in chiral wavenumber with temperature.[13] Purely steric interactions may also result in cholesteric phases, as predicted by theory[14–20] and confirmed by simulation.[21] Interestingly, for the specific case of helical rods, the handedness of the cholesteric phase was found to spontaneously change upon variation of the particle concentration alone.[17,22,23] It is clear at least that there are several competing microscopic mechanisms which control the formation of cholesteric phases. As illustrated by the latter example, simulations offer a convenient method by which to investigate a single mechanism in isolation. One of the first tasks when planning to simulate chiral liquid-crystals is selecting what attributes we wish to include in the intermolecular interactions.

Steric chirality may be studied by fusing multiple achiral centres to create new and interesting chiral interactions. Due to the straightforward nature of such models, the literature contains a variety of examples. Contacting pairs of Gay-Berne,[24,25] or hard Gaussian overlap particles,[14] aligned at fixed angles in each case, give rise to cholesteric phases. While the former case does have an attractive component to the pair potential, it is the spatial arrangement of the Gay-Berne centers that gives rise to the chiral interaction. Likewise, rigid assemblies of athermal hard, or soft repulsive, spheres may be used to model helices,[26,27] or simple enantiomeric mixtures,[28] while twisted polyhedra were used to generate purely entropy-driven cholesteric phases.[21] Similarly, in an effort to model the cholesteric phase of cellulose nanocrystals, a hard-splinter model composed of fused spherocylinders was explored recently.[29]

Simulating electrostatic chirality may be achieved in several ways: by creating bespoke coarse-grained models, which are suitable for complex molecules;[6,23,27] by using computationally efficient simple lattice[30–33] and off-lattice[33–35] models; by modification of existing achiral potentials, such as the chiral Gay-Berne potential;[36,37] and by all-atom models, although the latter is by far the most computationally expensive. There are also approaches that include the combination of a hard repulsive core with chiral electrostatics.[38] Interaction models such as these, pairing a hard body with an attractive potential, are noteworthy because the decoupling of attractive and repulsive forces allows a detailed study of their separate contributions to the phase behaviour. Previous examples, such as achiral rods[39–43] and disk-like particles,[44] provide valuable insight into the relative contributions of these separate forces to the overall phase behaviour of these fluids. A further advantage of decoupling attractive and repulsive contributions is that the challenging task of creating theoretical models[45–48] is somewhat simplified.

In nature, the pitch distance of cholesteric phases of liquid-crystals is typically on the order of 10-100 times the particle size. Understandably, with even the most computationally efficient simulations, one does not simply contain the half-pitch distance of such fluids within a single simulation box. The use, therefore, of standard periodic boundaries poses a particular problem for the simulation of cholesteric phases.[49] There are several ways to address this issue, the first of which is by the use of twisted

periodic boundaries.[50–52] The rotation of periodic images, in one axis only, through a right angle, forces the system to adopt twisted equilibrium structures. This is a useful approach for cases where the longest system length is 25% of the equilibrium pitch distance,[51] which should ideally be known *a priori*. However, while this approach does alleviate the aforementioned problem to a degree, it leaves the simulation of large pitch distances out of reach. Another approach to simulating systems with helical rotation is that of Memmer.[36] In their simulations of chiral Gay-Berne molecules, the utilisation of the isobaric-isothermal ensemble allows the simulation box dimensions to fluctuate such that the length of each axis changes independently. Provided the equilibrium half-pitch distance is within the range of possible domain lengths, this approach allows equilibrium pitch distances to be measured. Unfortunately, this is another method which, even when combined with twisted periodic boundaries, is not suitable for systems with large pitch distances, or for those where it is not known *a priori*. In the first case, the required system would be too large to simulate in a reasonable time frame and, in the second case, the predefined rotation at the twisted boundaries along the helical axis would not give the correct equilibrium pitch distance.

In the Monte Carlo simulation study by Varga and Jackson,[38] the difficulty of simulating large pitch distances with periodic boundaries was eliminated by the use of parallel hard walls, positioned at opposite ends of the helical axis. The introduction of such walls breaks the system's symmetry and introduces surface tension. It is necessary therefore to ensure that the distance between the surfaces is far enough to allow for the formation of a stable bulk region with constant local density and helical rotation. Provided this criterion is met, it appears this is the most favourable way of simulating cholesteric phases with large pitch distances. This approach has also seen use in the excellent simulation studies of sterically chiral molecules by Dussi and Dijkstra[21] and Wu and Sun[53] and is the method we shall employ in the present work on cholesteric phases of liquid crystals.

The remaining sections of this paper are presented in the following order: the molecular model of Wensink and Jackson[46] is detailed in section 2; in section 3, we summarise the theoretical relations derived by Wensink and Jackson;[46] our simulation settings and results for a cholesteric liquid-crystal fluid confined between planar walls are presented in section 4; a modified approach is taken in section 5 with so-called chiral walls; and in section 6 we make concluding remarks.

2 Intermolecular pair potential

The pair potential used in this work originates from the combination of the chiral dispersion term of Goossens[54] with a purely-repulsive hard-spherocylinder core — a cylinder with two hemispherical caps. This was first used in the Monte Carlo study of Varga and Jackson[38] to simulate cholesteric liquid-crystalline fluids with large pitch distances. Here we follow the theoretical study of Wensink and Jackson,[46] where this pair potential was modified to include a temperature dependency:

$$\frac{U_{ij}}{k_BT}=\begin{cases} 0; & \text{if } r_{ij}\geq L+D \\ -\dfrac{1}{T^*}\left(1+\epsilon_c\left(\left(\hat{\omega}_i\times\hat{\omega}_j\right)\cdot\hat{\omega}_{ij}\right)\left(\hat{\omega}_i\cdot\hat{\omega}_j\right)\right); & \text{if } \sigma\leq r_{ij}<L+D \\ \infty; & \text{if } r_{ij}<\sigma, \end{cases} \tag{1}$$

where k_BT is the thermal energy with k_B denoting Boltzmann's constant and T absolute temperature, L is the cylinder length, D is the diameter of the cylinder and of the hemispherical caps, ϵ_c the chiral strength parameter, $\hat{\omega}_i$, $\hat{\omega}_j$ and r_{ij} respectively denote the orientation unit vectors and centre-of-mass distance of molecules i and j. The unit vector oriented through the centre points of those molecules is $\hat{\omega}_{ij}$ and $\sigma(\hat{\omega}_i,\hat{\omega}_j,\hat{\omega}_{ij})$ is the distance between the centres of molecules i and j at the point of contact of the hard spherocylinder bodies. To take into account the effect of achiral attractive forces, the interparticle potential features an additional achiral square-well (SW) contribution with amplitude ϵ_0 that is subsumed into an effective temperature that we define as $T^*=$

k_BT/ϵ_0. The way in which the electrostatic forces change according to molecule positions and orientations in presented in figure 1. It is important to note that the SW chiral potential is long-ranged as its range scales with the total spherocylinder length $L + D$. This is in contrast to the one originally proposed by Goossens which decays much more rapidly with centre-of-mass distance, namely via $1/r_{ij}^7$. As such, the original Goossens potential is well-suited to address short-ranged chiral forces such as those imparted by the chiral shape of the mesogen, whereas the current one encapsulates chiral forces transmitted through long-ranged electrostatic forces whose range strongly exceeds the typical rod diameter. In this particular model, which is interesting from a theoretical perspective, it should be mentioned that these interactions are most significant for rod pairs in side-by-side configurations, with the dispersion interactions being zero for end-to-end configurations. As a final point of note about this potential, if ϵ_c becomes negative then the handedness of the chiral spherocylinder is switched.

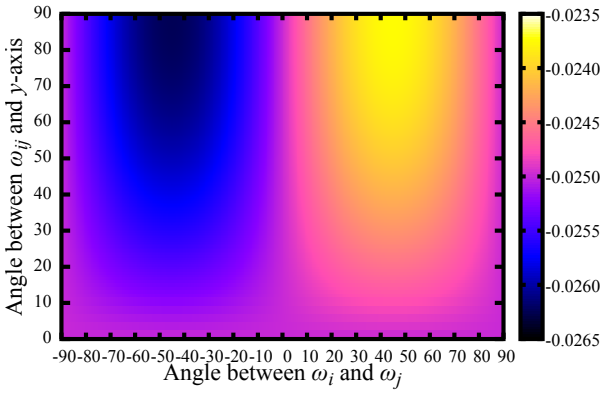

Figure 1: Contour plot of the electrostatic contributions from equation 1. $\hat{\omega}_i$, $\hat{\omega}_j$ and r_{ij} respectively denote the orientation unit vectors and centre-of-mass distance of molecules i and j. $\hat{\omega}_j$ is fixed along the x-axis and the particle i is free to rotate and translate within the cut-off distance of $L+D$. Values given correspond to a temperature of $T^* = 40$ and the chiral strength parameter of $\epsilon_c = 0.1$.

3 Wensink and Jackson's theoretical model for chiral spherocylinders

The theoretical model of Wensink and Jackson[46] relates the pitch distance of a chiral spherocylinder fluid to its bulk packing fraction. Since we use the same molecular model here, the predicted pitch distances and wavenumbers from that work are useful for comparison with our numerical results. By making a Gaussian approximation of the orientation distribution function applied within a mean-field Onsager-Parsons theory adapted for cholesteric fluids, they derived an analytical expression for the pitch distance in terms of the chiral interaction strength ϵ_c, packing fraction η and spherocylinder length L and diameter D:

$$P = \frac{L}{\bar{\epsilon}}\left(\frac{T^*}{\eta}\left(\frac{7\pi}{32} + \frac{24\kappa\eta^2}{\sqrt{\pi}}\left(G(\eta) + \frac{1}{T^*}\right)^2 + \mathcal{O}(D/L)\right)\right), \quad (2)$$

where the constant $\kappa = 0.036926$,

$$G(\eta) = \frac{1 - \frac{3}{4}\eta}{(1-\eta)^2}, \quad (3)$$

and

$$\bar{\epsilon} = \epsilon_c \frac{L}{D}\left(\frac{L+D}{L}\right)^4. \quad (4)$$

We note that in the original paper of Wensink and Jackson[46] there was a small typographical mistake in equation 4 which was later corrected. In the prior version, the inverse length-to-diameter ratio was squared in error. The equations we present here are in their correct form. By substitution and disregarding the higher order terms $\mathcal{O}(D/L)$, they arrived at:

$$P = \frac{D}{\epsilon_c\left(\frac{L+D}{L}\right)^4}\frac{T^*}{\eta}\left(\frac{7\pi}{32} + \frac{24\kappa\eta^2}{\sqrt{\pi}}\left(\frac{1-\frac{3}{4}\eta}{(1-\eta)^2} + \frac{1}{T^*}\right)^2\right). \quad (5)$$

It is worth mentioning that by neglecting the $\mathcal{O}(D/L)$ contributions this mean-field theory only applies to sufficiently elongated rods with $L/D \gg 1$. Further, smectic order and pre-smectic fluctuations are not considered.

Nonetheless, this gives a convenient expression for the pitch distance in terms of temperature and density for chiral spherocylinders of a given aspect ratio and chiral strength. An attractive feature of this model is that it allows representation of molecular liquid-crystals at low temperatures. At high temperatures, it is also a suitable model for colloidal liquid-crystals where interparticle attractions are typically less important. As expected, the pitch distance drops monotonically with increasing chiral amplitude ϵ_c and, for the range of effective temperatures T^* considered in this work, the pitch distance rises monotonically with increasing temperature. Variation in the packing fraction η leads to more complicated behaviour as we will see later.

In this work, the rod packing fraction is defined as $\eta = Nv_0/V$ with $v_0 = \pi LD^2/4 + \pi D^3/6$ the spherocylinder volume. Finally, we will express pitch distances and chiral wave numbers in reduced units, normalised by the rod length L: $P^* = P/L$, $q^* = 2\pi/P^*$. It is worth noting that the chiral wave number is ill-defined in the isotropic phase. It may however still be calculated and serves to show any residual helical rotation that the nematic ordering director has, on average, which is normally non-existent in an isotropic phase of non-chiral molecules.

4 Monte Carlo simulations of chiral spherocylinders confined between hard planar walls

4.1 Simulation methodology

Constant NVT simulations were performed for two types of systems, one for short chiral spherocylinders with an aspect ratio characterised by $L/D = 5$, and the other for long rods with $L/D = 10$. The density of each system was controlled by fixing the number of molecules, N, which are initially arranged in ideal crystal-lattice structures, with their centre-of-mass positions scaled isotropically to fill the available volume as uniformly as possible. Following prior works,[21,38,53,55] hard planar walls were positioned at the upper and lower limits of the z-axis, while standard periodic boundaries were imposed in the x- and y-axes. The two hard and featureless walls, parallel to each other and the x-y plane, confine the fluid. The presence of these walls at the upper and lower limits of the domain's z-axis breaks the symmetry of molecule-molecule interactions in the volumes adjacent to the walls.

From a steric perspective, a portion of the rod-rod interactions that would have been present in a bulk system is replaced by rod-wall interactions. Molecules within the rod-wall interaction range favour a closer alignment to the x-y plane of the wall than those molecules in the bulk. This is actually a helpful feature for the study of the cholesteric phase because it allows us to preselect the axis of rotation of the equilibrium states. Knowing, in advance, that any helical rotation will be in the z-axis means that the calculation of the bulk wave number and pitch distance is straightforward. Furthermore, as previously mentioned, the pitch distance itself is not predetermined. These two features are the key advantages of simulating chiral fluids under confinement. An example of the cholesteric phase from our simulations can be found in figure 2.

In the case of short rods ($L/D = 5$), the x and y domain lengths were set to $L_x = L_y = 30$, and the distance between the walls in the z-axis is set to $L_z = 37$, with all distances given in units of spherocylinder diameters. For the long ones ($L/D = 10$), these distances were $L_x = L_y = 35$ and $L_z = 51$. To test for system size effects, and to help with the smectic order parameter calculation for the long rods, we also performed additional simulations with a larger system with dimensions $L_x = L_y = 70$ and $L_z = 51$.

The parameters investigated in this section are varied between the two types of systems. For the short rods, the number of molecules, N, ranged from 1600 to 4600, in increments of $\Delta N = 100$, the chiral strength parameter, $\epsilon_c =$ 0.10, 0.40, 0.60, 0.80, and 1.00, while the temperature was set to $T^* = 40$. This indicates that rod-rod attractions are relatively weak, namely more than an order of magnitude smaller than

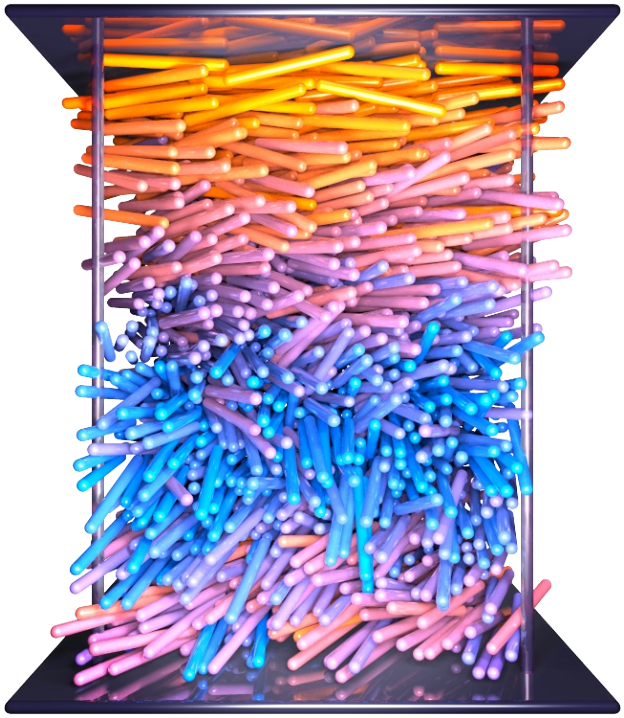

Figure 2: An example of a simulated system of chiral spherocylinders, with an aspect ratio characterised by $L/D = 10$, in the cholesteric phase. Variations in colour highlight differing molecular orientations.

the thermal energy k_BT. Similarly, for the long rods: $N = 1600$ to 3200; $\epsilon_c = 0.10$, 0.15, 0.40, 0.60, 0.80, and 1.00; at $T^* = 30$, 40, and 60.

Equilibrium configurations were obtained by performing 4×10^6 Monte Carlo cycles. Within each cycle, N translation and rotation moves are attempted. Representative snapshots of selected equilibrium configurations are presented in figures 3 and 4 for short and long chiral spherocylinders, respectively. From these equilibrium states, a further 12×10^6 Monte Carlo cycles were used to measure and record local values corresponding to local density and local orientational order.

Local density profiles, as a function of the distance between the wall surfaces, along the z-axis were calculated by dividing the system into bins of equal volume, stacked adjacent to one another and parallel to the confining walls, and counting the average number of molecules within each. In addition, for each of these bins, local nematic ordering directors were calculated and the projection of these directors onto the x-y plane was recorded. This approach has previously been used to accurately measure the equilibrium pitch distances of similar confined systems.[21,55] By comparison of orientational differences of the local nematic director in the x-y plane, for adjacent slabs, one may extrapolate this rotation to determine local pitch distances (P_b^*) and chiral wavenumbers (q_b^*), in the bulk of the system. In addition, we also calculate the local values of the smectic order parameter (τ_b) within the bulk region of the system. This is defined as

$$\tau_\mathrm{b} = \max\left(\langle \cos 2\pi d/l \rangle\right), \qquad (6)$$

where d is the distance between the centres of two particles in the axis normal to the plane of smectic layering and l is the layer spacing that maximises the value of τ_b. For the two limiting cases, τ_b will be unity for perfect local smectic order and zero when no local smectic order is present. Since l is not known *a priori* it must be found after collecting all data for d distances. An iterative method is employed to determine the value of l which maximises τ_b for each local bin in each configuration sampled. The bulk value is then taken as the average of those bins in the bulk of the system.

For systems where the wall separation distance is sufficiently long, there will be regions between the two walls where the local pitch distances, wavenumbers and smectic order parameter values are invariant with z. These are taken to be the equilibrium values of the bulk phase for each of the simulated conditions.

4.2 Results

An important consideration with all confined systems is to establish the range of surface effects away from the surface. That is the distance beyond which the surfaces cease to influence the phase behaviour of the fluid. The region of the system which is further away from the surfaces than this distance is expected to have the same properties as those of bulk systems of the same density and temperature. Since we are principally interested in the bulk phase behaviour of chiral fluids it is therefore

essential we know precisely the location of this bulk region.

One way of establishing the location of bulk fluid regions is to examine local density profiles. The bulk fluid is expected to have a density which is invariant with its distance from either surface. For this purpose, local density profiles for confined systems of short and long chiral spherocylinders are presented in figures 5 and 6, respectively.

The previous plots show that the density profiles do not change appreciably with chiral strength for the shorter rods. In the case of the longer rods, we see less wall structure at higher temperatures. Importantly we also have density invariance in the bulk of the system. However, we need to ensure that the helical rotation of the pitch distance is also constant within that region.

To this end, we present an example plot of local angular rotation of the nematic ordering director between neighbouring bins for the short rods in figure 7. Each bin is $\frac{1}{20}$th of the total distance between the surfaces. These angles of rotation are used to compute the local wavenumbers for selected systems for the two aforementioned aspect ratios in figures 8 and 9. Again, we may observe density invariance in the middle, or bulk, of each system. As expected, we see isotropic-nematic phase transitions at bulk packing fractions of $\eta_b = 0.35 \leftrightarrow 0.45$ for the shorter rods and $\eta_b = 0.25 \leftrightarrow 0.30$ for the longer rods. These phase transition points are significantly higher than those of their non-chiral and purely repulsive hard-spherocylinder counterpart fluids. For the long rods the isotropic-nematic phase transition occurs at $\eta_b = 0.25 \leftrightarrow 0.275$[56] while for the short rods these have been reported to be $\eta_b = 0.24 \leftrightarrow 0.27$.[57] In the latter case, we expect to see the smectic phase at around $\eta_b = 0.48$.[58] It is also interesting to note how the wall-wetting properties differ between the two rod-lengths studied in this work, particularly at high bulk densities. It is apparent that, at high bulk densities, the longer rods wet the walls with a cholesteric film while the bulk of the system has already transitioned to a smectic phase, which is characterised by a near-zero wavenumber. The shorter rods on the other hand do not exhibit this type of behaviour and are, by comparison, much more homogeneous between the surfaces. Further inspection of figures 5, 6, 8 and 9 also reveals a surface drying effect where the rods are locally less nematic at distances less than a rod length from the wall. This is to be expected with walls that are purely repulsive. Finally, it is worth noting that we would anticipate that the shorter rods will develop smectic signatures in the bulk more easily than the longer ones given that the window of stability of the nematic bulk phase is much narrower for shorter rods.[59,60]

Having established the bulk regions of density and wavenumber invariance for each of our simulated systems we now compare the simulated bulk phase properties with those predicted by theoretical methods. In figures 10 and 11 we plot bulk wave numbers versus bulk packing fraction for our Monte Carlo simulations alongside predictions obtained from the theory of Wensink and Jackson.[46] A clear and qualitative agreement is found with a non-monotonic relationship between bulk density and wavenumber in all cases. Regarding quantitative comparison, we see a reasonable agreement in both cases for higher values of ϵ_c. Our simulation results are supported by prior experimental work; suspensions of filamentous bacteriophages (*fd* virus) exhibit a similar non-monotonic relationship between the wavenumber and virus density.[61] As expected, we are also able to find agreement with the findings of Ogolla et al.[13] and see a decrease in chiral wavenumber with temperature in figure 9 for the low-density cholesteric phase.

In figure 12 we reproduce the simulation results for the short chiral spherocylinders, this time including data for the smectic order parameter (τ_{b}). Here, we observe an apparent increase in smectic order occurring concurrently with an unwinding of the cholesteric helix. Prior simulation work had shown a small increase in smectic ordering before the cholesteric to smectic phase transition,[37] but it was unclear if this occurred concurrently with the unwinding of the cholesteric helix. In the section that follows we will investigate this question in more

detail. We will note here that of the smectic states found at the higher end of the density range, we observed them to be in the smectic-A phase.

It is important also to check for system size effects. To this end we performed additional simulations for the longer rods with larger systems as described in the previous section. The density profiles can be found in figure 13. Again we see density invariance in the bulk of the system and so we may use this region to calculate bulk properties. These larger systems also allow us to calculate the smectic order parameter. With the previously discussed simulations of the longer rods there were too few molecules in each of the local bins to adequately measure τ_{b}. In figure 14 we plot this along with the bulk wave number. Here it is clear that the increase in smectic ordering is much more subtle and does not necessarily coincide with a fall in wave-number. It seems at least on the basis of these results that perhaps pre-smectic fluctuations play a more significant role in the unwinding helix for shorter rods.

5 Monte Carlo simulations of chiral spherocylinders confined between chiral walls

5.1 Chiral walls

While the results in the previous section would seem to suggest a simultaneous increase in smectic ordering and cholesteric helix unwinding with increasing density we feel that a more thorough analysis is required to confirm if this is indeed the case. Furthermore, we wish to investigate this behaviour at lower and more realistic temperatures to better represent liquid-crystal fluid phase behaviour in thermotropic, low-molecular-weight liquid crystals. However, this poses a problem concerning our choice of molecule-surface interaction model. At lower temperatures, a purely repulsive surface cannot compete with stronger intermolecular forces and we observed frequent droplet formation in the centre of the system coupled with a pronounced surface drying effect. This is due to an imbalance of interactions for molecules close to the walls due to the absence of molecules in the volume beyond the wall surface. To address this issue we need to correct for the breaking of molecule-molecule interaction symmetry near the surfaces.

To this end, in the second part of this work we turn our attention towards a different type of molecule-surface interaction. While retaining the molecular pair potential of Wensink and Jackson,[46] and the hard surface we used in the previous section, we make changes to the way the pair potentials are calculated for molecules close to the surfaces.

This new method is computationally efficient and works in the same way as described previously, with one alteration. When, for example, molecule A interacts electrostatically with another molecule, B, an additional check is made. Firstly, we draw an imaginary mirror plane that is parallel to the surface of the walls and intersects the centre of molecule A. If the mirror image reflection of molecule B in this mirror plane is fully outside of the walls, we double the pair potential between molecules A and B. A visualisation of the way these interactions work is given in figure 15.

In this manner, we are able to mimic the effect of there being molecules beyond the wall surface with the same electrostatic influence and packing fraction as the molecules within the system. We also retain the advantages given by planar walls for simulating a stable chiral twist in the z-axis normal to the wall surface.

The effect of imposing these domain boundaries is that molecules near the chiral walls feel the presence of molecules beyond the surface and are subject to similar chiral electrostatics as they are from molecules which are further away from the wall. This lessens the symmetry-breaking properties of the wall and promotes more uniform local wavenumbers throughout the domain. It also gives the wall a pseudo-attractive property which has the added benefit of preventing surface drying and subsequent droplet formation in the bulk of the system. These are desirable as we wish to ensure that

the cholesteric helix is orientated along the z-axis for our measurements.

As a word of caution, it should be noted however that this surface interaction model is only appropriate for more highly ordered liquid-crystals phases. Isotropic phases do not play well with this type of boundary. Fortunately, for our purposes, this is not a problem as our interest lies in the highly ordered cholesteric and smectic phases and the transition between them.

As before, constant NVT simulations were performed for chiral spherocylinders with an aspect ratio characterised by $L/D = 5$ for a range of system densities. This time we set the temperature to a lower value of $T^* = 10$ to represent a more realistic scenario for liquid crystal behaviour. As described above, we implement chiral walls at the upper and lower z domain boundaries.

Using this setup we performed Monte Carlo simulations of these systems for 6×10^6 cycles to attain equilibrium states and then a further 18×10^6 cycles over which bulk averages of density, wavenumber and smectic order parameter values were calculated.

The results from our simulations with chiral walls are plotted in figures 16, 17 and 18. In the case of the first two, we again see invariance of the density and wave number in the bulk of the system. While the latter figure gives us a much clearer picture of the density dependence of both the wavenumber and smectic order parameter in the bulk regions of the simulated systems. Following our results in the previous section, we find a simultaneous onset of increasing smectic ordering with decreasing wavenumber, starting at $\eta_b \approx 0.455$. We believe that our results here indicate that a driving force behind the unwinding of the cholesteric helix at higher densities is enhanced pre-smectic ordering which occurs well before the cholesteric-to-smectic phase transition in the bulk.

6 Conclusions

Following the simulation study of Varga and Jackson,[38] we have taken advantage of the symmetry-breaking properties of hard walls to simulate cholesteric liquid-crystal fluids with large pitch distances in a computationally efficient manner. Taking measurements from only the bulk region of the system, we obtain estimates of the pitch distances as a function of chiral strength, system density, and temperature.

Results for two different spherocylinder aspect ratios are compared to the DFT predictions of Wensink and Jackson[46] and a qualitative agreement is found between the wavenumbers and density for a range of temperatures and chiral strength values. Although it must to stated that this agreement is not quantitative for the most part, with some improvement being present only for higher chiral strength values. Following the experiments of Ogolla et al.[13] and simulations of Varga and Jackson[38] we see similar decreases in wavenumber with temperature for the low-density cholesteric phase. We also find support from the experiments of Dogic and Fraden[61] in that the observed non-monotonic trend of increasing wavenumbers with density corresponds to the isotropic to cholesteric transition while, at a higher density, the decrease in wavenumbers is due to the cholesteric to smectic phase transition. For shorter rods, characterised by an aspect ratio of $L/D = 5$, we find evidence that, at low temperatures, this unwinding of the cholesteric helix is driven by pre-smectic fluctuations within the cholesteric phase. This latter point is in contradiction to prior theoretical predictions,[46] which is not unexpected since it was based on the assumption of a uniform nematic with the absence of smectic ordering. We further remark that a similar non-monotonic relationship between the pitch and rod density has been reported from theories for cholesteric phases of rods with a distinct helical shape, again without smectic fluctuations included.[17,22] A non-monotonic variation of the pitch with rod density has been observed in simulations of helical rods but the role of local smectic order was not considered there.[23] In all these cases, the non-monotonic dependence of the pitch with concentration was attributed entirely to the distinctly helical architecture of the rods, whereas in our model

the rods are chiral but not necessarily helical. A further discrepancy with systems dominated by short-ranged shape chirality relates to the fact that the chiral intermolecular interactions in our model are long-ranged while the typical chiral interaction energy ϵ_c/T^* is about two orders of magnitude smaller than the thermal energy, suggesting that the chiral forces underpinning the non-monotonic variation of the pitch with density we observe are very weak indeed.

Further work will be necessary to determine if the relationship observed here holds for longer rods at high temperatures which is relevant for entropy-stabilized colloidal liquid crystals. The experimental observations of Dogic and Fraden[11] demonstrated that very long ($L/D \approx 130$) and purely repulsive virus suspensions have the cholesteric helix unwinding before the onset of local smectic order at high temperatures. As hinted at by our preliminary results for the longer rods, it would be intriguing to see if it were possible to simulate this separation of cholesteric helix unwinding from smectic fluctuations for rods experiencing long-range chiral forces, such as those represented in our model. This would lend further support to the theoretical work of Wensink and Jackson[46] where the unwinding cholesteric helix is driven by a subtle scaling of the collective chiral strength and the twist elastic modulus with rod concentration, without the need to invoke local smectic order or steric chirality imparted by some helical rod shape. While it would also be of interest to investigate chiral systems of polydisperse rod lengths and make contact with theoretical[62] progress. Since polydispersity destabilises smectic ordering this would allow us to investigate how the pitch behaves with far less interference from local smectic structures. As a final point, it would be interesting to explore the possibility of recasting the aforementioned DFT to probe the cholesteric-to-smectic transition, as this may provide an improved prediction of the higher density behaviour.

Acknowledgement The authors thank George Jackson and Andrew Haslam for fruitful discussions on this topic. The authors declare that they have no known competing financial interests or personal relationships that could have appeared to influence the work reported in this paper. Data will be made available on request.

References

(1) Harris, A. B.; Kamien, R. D.; Lubensky, T. C. Molecular chirality and chiral parameters. *Rev. Mod. Phys.* **1999**, *71*, 1745–1757.

(2) Sharma, V.; Crne, M.; Park, J. O.; Srinivasarao, M. Structural Origin of Circularly Polarized Iridescence in Jeweled Beetles. *Science* **2009**, *325*, 449–451.

(3) Mitov, M. Cholesteric liquid crystals in living matter. *Soft Matter* **2017**, *13*, 4176–4209.

(4) Kornyshev, A. A.; Leikin, S. Twist in Chiral Interaction between Biological Helices. *Phys. Rev. Lett.* **2000**, *84*, 2537–2540.

(5) Yevdokimov, Y. M.; Skuridin, S. G.; Salyanov, V. I. The Liquid-Crystalline Phases of Double-Stranded Nucleic Acids in Vitro and in Vivo. *Liq. Cryst.* **1988**, *3*, 1443–1459.

(6) Tombolato, F.; Ferrarini, A. From the double-stranded helix to the chiral nematic phase of B-DNA: A molecular model. *J. Chem. Phys.* **2005**, *122*, 054908.

(7) Tombolato, F.; Ferrarini, A.; Grelet, E. Chiral Nematic Phase of Suspensions of Rodlike Viruses: Left-Handed Phase Helicity from a Right-Handed Molecular Helix. *Phys. Rev. Lett.* **2006**, *96*, 258302.

(8) Barry, E.; Hensel, Z.; Dogic, Z.; Shribak, M.; Oldenbourg, R. Entropy-Driven Formation of a Chiral Liquid-Crystalline Phase of Helical Filaments. *Phys. Rev. Lett.* **2006**, *96*, 018305.

(9) Grelet, E.; Fraden, S. What Is the Origin of Chirality in the Cholesteric Phase of Virus Suspensions? *Phys. Rev. Lett.* **2003**, *90*, 198302.

(10) Barry, E.; Beller, D.; Dogic, Z. A model liquid crystalline system based on rodlike viruses with variable chirality and persistence length. *Soft Matter* **2009**, *5*, 2563–2570.

(11) Dogic, Z.; Fraden, S. Cholesteric Phase in Virus Suspensions. *Langmuir* **2000**, *16*, 7820–7824.

(12) Dogic, Z.; Fraden, S. Ordered phases of filamentous viruses. *Curr. Opin. Colloid Int. Sci.* **2006**, *11*, 47–55.

(13) Ogolla, T.; Paley, R. S.; Collings, P. J. Temperature dependence of the pitch in chiral lyotropic chromonic liquid crystals. *Soft Matter* **2019**, *15*, 109–115.

(14) Varga, S.; Jackson, G. A study of steric chirality: the chiral nematic phase of a system of chiral two-site HGO molecules. *Mol. Phys.* **2011**, *109*, 1313–1330.

(15) Belli, S.; Dussi, S.; Dijkstra, M.; van Roij, R. Density functional theory for chiral nematic liquid crystals. *Phys. Rev. E* **2014**, *90*, 020503.

(16) Frezza, E.; Ferrarini, A.; Bindu Kolli, H.; Giacometti, A.; Cinacchi, G. Left or right cholesterics? A matter of helix handedness and curliness. *Phys. Chem. Chem. Phys.* **2014**, *16*, 16225–16232.

(17) Dussi, S.; Belli, S.; van Roij, R.; Dijkstra, M. Cholesterics of colloidal helices: Predicting the macroscopic pitch from the particle shape and thermodynamic state. *J. Chem. Phys.* **2015**, *142*, 074905.

(18) Wensink, H. H.; Morales-Anda, L. Chiral assembly of weakly curled hard rods: Effect of steric chirality and polarity. *J. Chem. Phys.* **2015**, *143*, 144907.

(19) De Michele, C.; Zanchetta, G.; Bellini, T.; Frezza, E.; Ferrarini, A. Hierarchical Propagation of Chirality through Reversible Polymerization: The Cholesteric Phase of DNA Oligomers. *ACS Macro Lett.* **2016**, *5*, 208–212.

(20) Tortora, M. M. C.; Doye, J. P. K. Hierarchical bounding structures for efficient virial computations: Towards a realistic molecular description of cholesterics. *J. Chem. Phys.* **2017**, *147*, 224504.

(21) Dussi, S.; Dijkstra, M. Entropy-driven formation of chiral nematic phases by computer simulations. *Nature Commun.* **2016**, *7*, 11175.

(22) Wensink, H. H. Spontaneous sense inversion in helical mesophases. *Europhys. Lett.* **2014**, *107*, 36001.

(23) Růžička, S.; Wensink, H. H. Simulating the pitch sensitivity of twisted nematics of patchy rods. *Soft Matter* **2016**, *12*, 5205–5213.

(24) Memmer, R.; Kuball, H.-G.; Schönhofer, A. Computer simulation of chiral liquid crystal phases. IV. Intermolecular chirality transfer to rotamers in a cholesteric phase. *Liq. Cryst.* **1995**, *19*, 749–753.

(25) Memmer, R. Liquid crystal phases of achiral banana-shaped molecules: a computer simulation study. *Liq. Cryst.* **2002**, *29*, 483–496.

(26) Frezza, E.; Ferrarini, A.; Kolli, H. B.; Giacometti, A.; Cinacchi, G. The isotropic-to-nematic phase transition in hard helices: Theory and simulation. *J. Chem. Phys.* **2013**, *138*, 164906.

(27) Kuhnhold, A.; Schilling, T. Isotropic-nematic transition and cholesteric phases of helical Yukawa rods. *J. Chem. Phys.* **2016**, *145*, 194904.

(28) Cao, M.; Monson, P. A. A study of the phase behavior of a simple model of chiral molecules and enantiomeric mixtures. *J. Chem. Phys.* **2005**, *122*.

(29) Chiappini, M.; Dussi, S.; Frka-Petesic, B.; Vignolini, S.; Dijkstra, M. Modeling the cholesteric pitch of apolar cellulose nanocrystal suspensions using a chiral

hard-bundle model. *J. Chem. Phys.* **2022**, *156*, 014904.

(30) Lombardo, T. G.; Stillinger, F. H.; Debenedetti, P. G. Thermodynamic mechanism for solution phase chiral amplification via a lattice model. *Proc. Natl. Acad. Sci.* **2009**, *106*, 15131–15135.

(31) Hatch, H. W.; Stillinger, F. H.; Debenedetti, P. G. Chiral symmetry breaking in a microscopic model with asymmetric autocatalysis and inhibition. *J. Chem. Phys.* **2010**, *133*.

(32) Ricci, F.; Stillinger, F. H.; Debenedetti, P. G. Creation and Persistence of Chiral Asymmetry in a Microscopically Reversible Molecular Model. *J. Phys. Chem. B* **2013**, *117*, 602–614.

(33) Skutnik, R. A.; Eichler, J.-C.; Mazza, M. G.; Schoen, M. The temperature dependence of the helical pitch in a cholesteric liquid crystal. *Mol. Phys.* **2021**, e1881638.

(34) Ricci, M.; Mazzeo, M.; Berardi, R.; Pasini, P.; Zannoni, C. A molecular level simulation of a twisted nematic cell. *Faraday Discuss.* **2010**, *144*, 171–185.

(35) Latinwo, F.; Stillinger, F. H.; Debenedetti, P. G. Molecular model for chirality phenomena. *J. Chem. Phys.* **2016**, *145*, 154503.

(36) Memmer, R. Determination of equilibrium pitch of cholesteric phases by isobaric-isothermal Monte Carlo simulation. *J. Chem. Phys.* **2001**, *114*, 8210–8222.

(37) Nozawa, T.; Brumby, P. E.; Yasuoka, K. Effect of Central Longitudinal Dipole Interactions on Chiral Liquid-Crystal Phases. *Int. J. Mol. Sci.* **2018**, *19*.

(38) Varga, S.; Jackson, G. Simulation of the macroscopic pitch of a chiral nematic phase of a model chiral mesogen. *Chem. Phys. Lett.* **2003**, *377*, 6–12.

(39) Gil-Villegas, A.; McGrother, S. C.; Jackson, G. Chain and ring structures in smectic phases of molecules with transverse dipoles. *Chem. Phys. Lett.* **1997**, *269*, 441–447.

(40) Gil-Villegas, A.; McGrother, S. C.; Jackson, G. Reaction-field and Ewald summation methods in Monte Carlo simulations of dipolar liquid crystals. *Mol. Phys.* **1997**, *92*, 723–734.

(41) Avendaño, C.; Gil-Villegas, A.; González-Tovar, E. Computer simulation of charged hard spherocylinders. *J. Phys. Chem.* **2008**, *128*, 044506.

(42) Jiménez-Serratos, G.; Avendaño, C.; Gil-Villegas, A.; González-Tovar, E. Computer simulation of charged hard spherocylinders at low temperatures. *Mol. Phys.* **2011**, *109*, 27–36.

(43) Viveros-Méndez, P. X.; Gil-Villegas, A.; Aranda-Espinoza, S. Monte Carlo computer simulation of sedimentation of charged hard spherocylinders. *J. Chem. Phys.* **2014**, *141*, 044905.

(44) Meneses-Juárez, E.; S. Varga, P. O.; Odriozola, G. Towards understanding the empty liquid of colloidal platelets: vapour-liquid phase coexistence of square-well oblate ellipsoids. *Soft Matter* **2013**, *9*, 5277.

(45) Wensink, H. H. Columnar versus smectic order in systems of charged colloidal rods. *J. Phys. Chem.* **2007**, *126*, 194901.

(46) Wensink, H. H.; Jackson, G. Generalized van der Waals theory for the twist elastic modulus and helical pitch of cholesterics. *J. Chem. Phys.* **2009**, *130*, 234911.

(47) Wu, L.; Jackson, G.; Müller, E. A. Liquid Crystal Phase Behaviour of Attractive Disc-Like Particles. *Int. J. Mol. Sci.* **2013**, *14*, 16414–16442.

(48) Wu, L.; Müller, E. A.; Jackson, G. Understanding and Describing the Liquid-Crystalline States of Polypeptide Solutions: A Coarse-Grained Model of PBLG in DMF. *Macromolecules* **2014**, *47*, 1482–1493.

(49) Frenkel, D. Simulations: The dark side. *Eur. Phys. J. Plus* **2013**, *128*, 10.

(50) Allen, M. P. Calculating the helical twisting power of dopants in a liquid crystal by computer simulation. *Phys. Rev. E* **1993**, *47*, 4611–4614.

(51) Allen, M. P.; Masters, A. J. Computer simulation of a twisted nematic liquid crystal. *Mol. Phys.* **1993**, *79*, 277–289.

(52) Germano, G.; Allen, M. P.; Masters, A. J. Simultaneous calculation of the helical pitch and the twist elastic constant in chiral liquid crystals from intermolecular torques. *J. Chem. Phys.* **2002**, *116*, 9422–9430.

(53) Wu, L.; Sun, H. Cholesteric ordering predicted using a coarse-grained polymeric model with helical interactions. *Soft Matter* **2018**, *14*, 344–353.

(54) Goossens, W. J. A. A Molecular Theory of the Cholesteric Phase and of the Twisting Power of Optically Active Molecules in a Nematic Liquid Crystal. *Mol. Cryst. Liq. Cryst.* **1971**, *12*, 237–244.

(55) Varga, S.; Jackson, G. Study of the pitch of fluids of electrostatically chiral anisotropic molecules: mean-field theory and simulation. *Mol. Phys.* **2006**, *104*, 3681–3691.

(56) Brumby, P. E.; Wensink, H. H.; Haslam, A. J.; Jackson, G. Structure and Interfacial Tension of a Hard-Rod Fluid in Planar Confinement. *Langmuir* **2017**, *33*, 11754–11770.

(57) Frenkel, D. Structure of hard-core models for liquid crystals. *J. Phys. Chem.* **1988**, *92*, 3280–3284.

(58) Frenkel, D. Onsager's spherocylinders revisited. *J. Phys. Chem.* **1987**, *91*, 4912–4916.

(59) McGrother, S. C.; Williamson, D. C.; Jackson, G. A re-examination of the phase diagram of hard spherocylinders. *J. Chem. Phys.* **1996**, *104*, 6755–6771.

(60) Bolhuis, P.; Frenkel, D. Tracing the phase boundaries of hard spherocylinders. *J. Chem. Phys.* **1997**, *106*, 666–687.

(61) Dogic, Z.; Fraden, S. Smectic Phase in a Colloidal Suspension of Semiflexible Virus Particles. *Phys. Rev. Lett.* **1997**, *78*, 2417–2420.

(62) Wensink, H. H. Polymeric Nematics of Associating Rods: Phase Behavior, Chiral Propagation, and Elasticity. *Macromolecules* **2019**, *52*, 7994–8005.

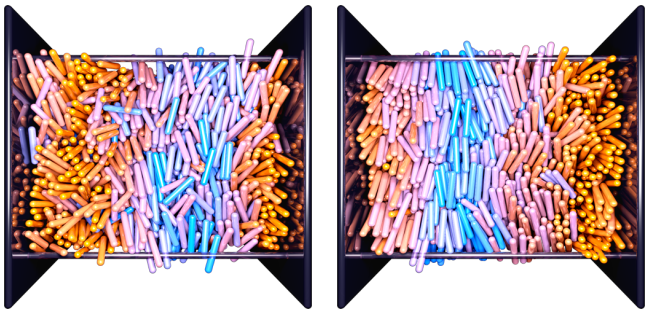

(a) $\eta_b = 0.431 \pm 0.001$, $q_b^* = 0.433 \pm 0.036$, $P_b^* = 14.52 \pm 1.08$.

(b) $\eta_b = 0.484 \pm 0.001$, $q_b^* = 0.307 \pm 0.048$, $P_b^* = 20.48 \pm 2.96$.

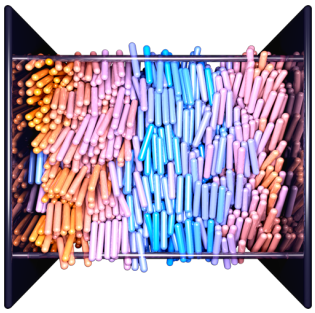

(c) $\eta_b = 0.510 \pm 0.001$, $q_b^* = 0.277 \pm 0.065$, $P_b^* = 22.67 \pm 4.81$.

Figure 3: Snapshots of simulated systems of chiral spherocylinders, with an aspect ratio characterised by $L/D = 5$. Variations in colour highlight differing molecular orientations. For all systems $\epsilon_c = 0.60$ and $T^* = 40$. Bulk density (η_b), bulk pitch distance (P_b^*), and bulk wavenumber (q_b^*) are as labelled. The dimensions of the system axes are $L_x/D = 30$, $L_y/D = 30$ and $L_z/D = 37$, where L_z is the separation distance between the hard parallel walls.

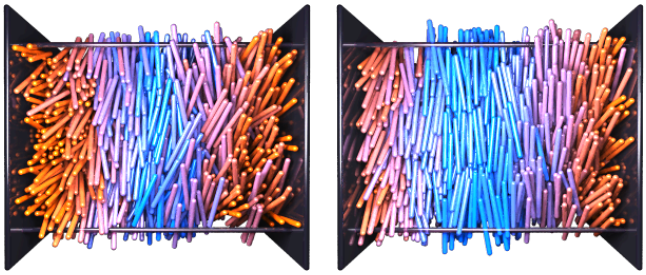

(a) $\eta_b = 0.340 \pm 0.001$, $q_b^* = 0.612 \pm 0.031$, $P_b^* = 10.27 \pm 0.52$.

(b) $\eta_b = 0.427 \pm 0.002$, $q_b^* = 0.367 \pm 0.023$, $P_b^* = 17.15 \pm 1.14$.

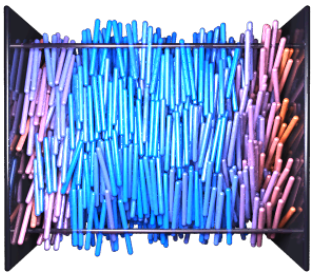

(c) $\eta_b = 0.450 \pm 0.002$, $q_b^* = 0.036 \pm 0.017$, $P_b^* = 174.14 \pm 65.35$.

Figure 4: Snapshots of simulated systems of chiral spherocylinders, with an aspect ratio characterised by $L/D = 10$. Variations in colour highlight differing molecular orientations. For all systems $\epsilon_c = 0.15$ and $T^* = 30$. Bulk density (η_b), bulk pitch distance (P_b^*), and bulk wavenumber (q_b^*) are as labelled. The dimensions of the system axes are $L_x/D = 35$, $L_y/D = 35$ and $L_z/D = 51$, where L_z is the separation distance between the hard parallel walls.

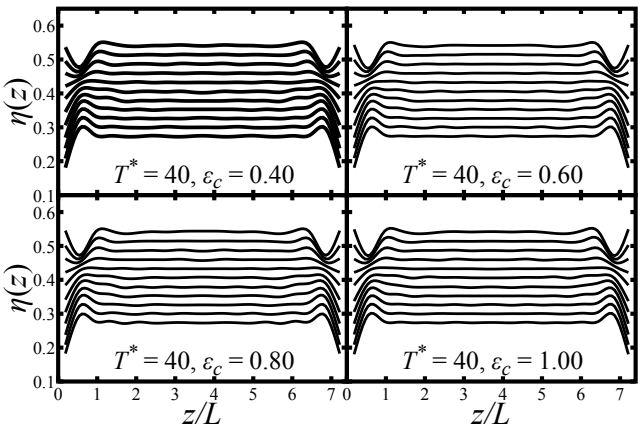

Figure 5: Plots of local packing fraction ($\eta(z)$) vs. distance from the lower wall (z, with distances in units of spherocylinder length), for systems of chiral spherocylinders, with an aspect ratio characterised by $L/D = 5$, and the addition of a chiral dispersion term, at a temperature of $T^* = 40$. Lines correspond to the local packing fractions for systems with differing system densities, with the number of molecules ranging from $N = 2000$ to $N = 4600$. The chiral strength parameter (ϵ_c) is labelled on each plot.

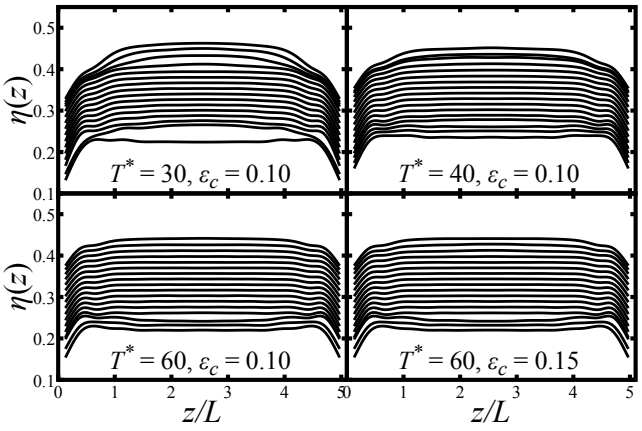

Figure 6: Same as figure 5 but for systems of chiral spherocylinders, with an aspect ratio characterised by $L/D = 10$ and the number of molecules ranging from $N = 1600$ to $N = 3200$. The temperature (T^*) and chiral strength parameter (ϵ_c) are labelled on each plot.

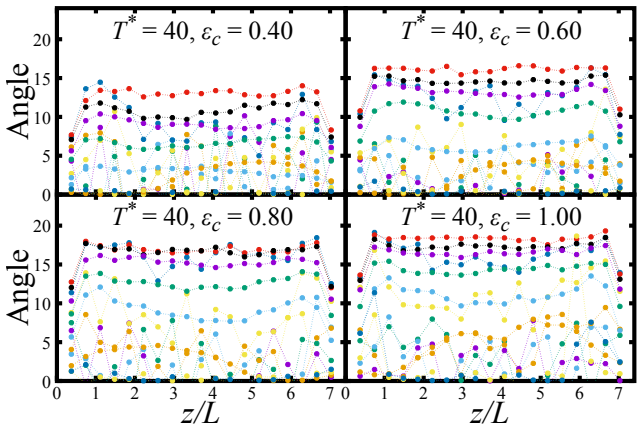

Figure 7: Plots of the local angular rotation of the nematic ordering director between neighbouring bins vs. distance from the lower wall (z, with distances in units of spherocylinder length), for systems of chiral spherocylinders, with an aspect ratio characterised by $L/D = 5$, and the addition of a chiral dispersion term, at a temperature of $T^* = 40$. Lines correspond to the local packing fractions for systems with differing system densities, with the number of molecules ranging from $N = 2000$ to $N = 4600$. The chiral strength parameter (ϵ_c) is labelled on each plot.

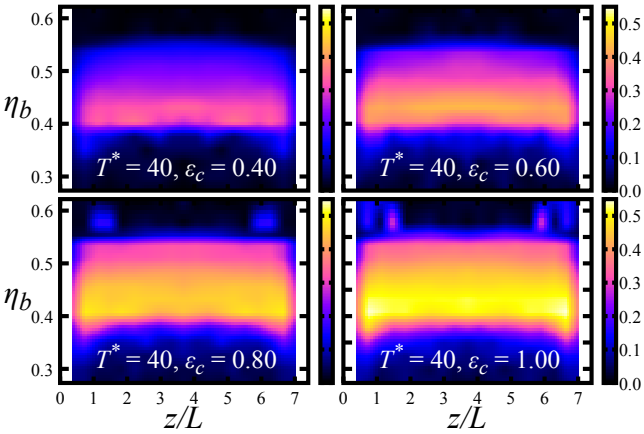

Figure 8: Contour plots of the local chiral wavenumber ($q^*(z)$), as a function of the bulk packing fraction (η_b), and distance from the lower wall (z, in units of spherocylinder length), for systems of chiral spherocylinders with an aspect ratio characterised by $L/D = 5$, and the addition of a chiral dispersion term, at a temperature of $T^* = 40$. The chiral strength parameter (ϵ_c) is labelled on each plot.

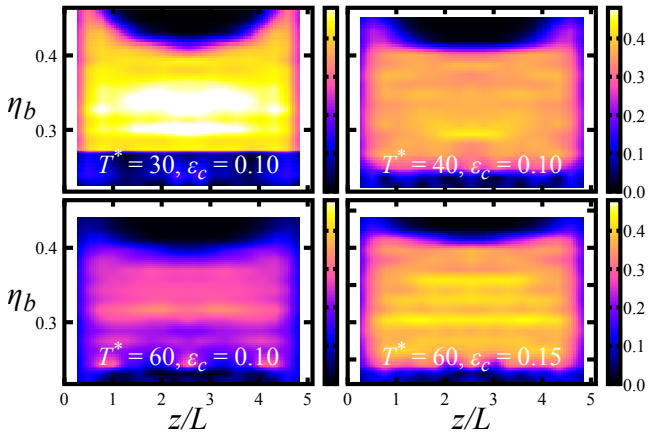

Figure 9: Same as figure 8 but for systems of chiral spherocylinders with an aspect ratio characterised by $L/D = 10$. The temperature (T^*) and chiral strength parameter (ϵ_c) are labelled on each plot.

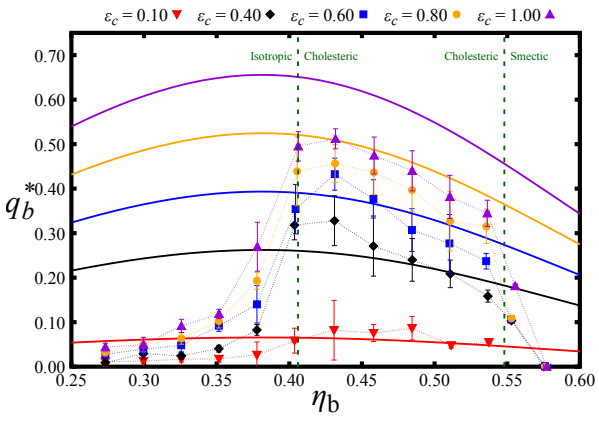

Figure 10: A plot of bulk wavenumber (q_b^*) versus bulk packing fraction (η_b), for systems of chiral spherocylinders with an aspect ratio characterised by $L/D = 5$ and the addition of a chiral dispersion term. The temperature $T^* = 40$. The chiral strength parameter, (ϵ_c) is labelled in the legend. Solid lines represent theoretical predictions using the analytical model of Wensink and Jackson[46] with these lines corresponding to points of the same colour from Monte Carlo simulations. The vertical green dashed lines and text indicate the approximate locations of the isotropic-to-cholesteric and cholesteric-to-smectic phase transition points.

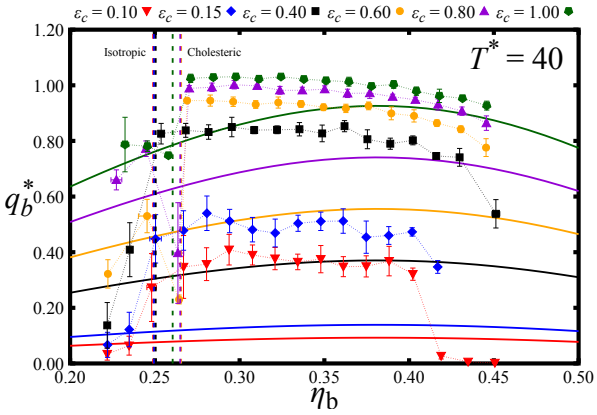

Figure 11: A plot of bulk wavenumber (q_b^*) versus bulk packing fraction (η_b), for systems of chiral spherocylinders with an aspect ratio characterised by $L/D = 10$ and the addition of a chiral dispersion term. The temperature $T^* = 40$ and the chiral strength parameters (ϵ_c) are as labelled in the legends. Solid lines represent theoretical predictions using the model of Wensink and Jackson[46] with these lines corresponding to points of the same colour from Monte Carlo simulations. The vertical dashed lines and text indicate the approximate locations of the isotropic-to-cholesteric phase transition point.

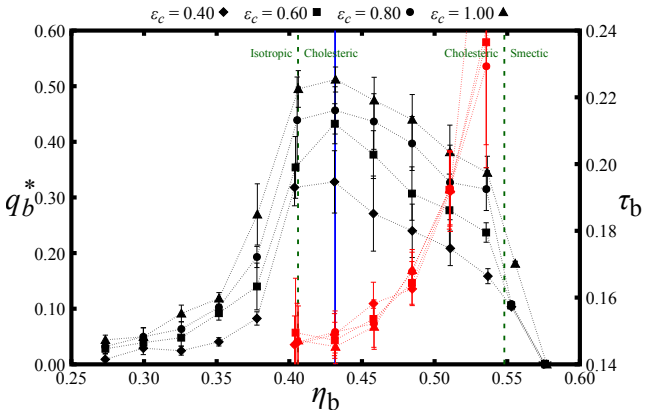

Figure 12: A plot of bulk wavenumber (q_b^*, black symbols) and smectic order parameter (τ_b, red symbols) versus bulk packing fraction (η_b), for systems of chiral spherocylinders with an aspect ratio characterised by $L/D = 5$ and the addition of a chiral dispersion term. The temperature $T^* = 40$. The chiral strength parameters (ϵ_c) are labelled in the legend. The vertical blue line indicates the bulk packing fraction above which we see a simultaneous increase in smectic ordering and unwinding of the cholesteric helix. The vertical green dashed lines and text indicate the approximate locations of the isotropic-to-cholesteric and cholesteric-to-smectic phase transition points.

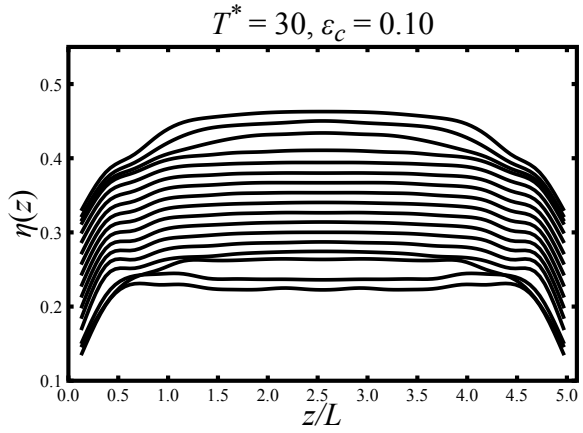

Figure 13: Same as figure 5 but for systems of chiral spherocylinders, with an aspect ratio characterised by $L/D = 10$ and the number of molecules ranging from $N = 6400$ to $N = 12800$. The temperature $T^* = 30$ and the chiral strength parameter $\epsilon_c = 0.1$.

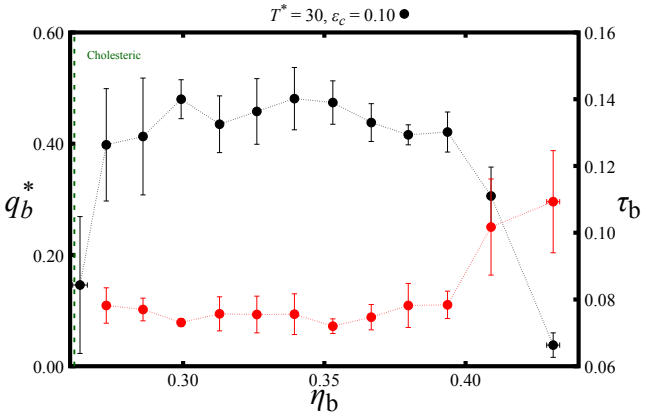

Figure 14: A plot of bulk wavenumber (q_b^*, black symbols) and smectic order parameter (τ_b, red symbols) versus bulk packing fraction (η_b), for systems of chiral spherocylinders with an aspect ratio characterised by $L/D = 10$ and the addition of a chiral dispersion term. The temperature $T^* = 30$ and the chiral strength parameter $\epsilon_c = 0.1$. The vertical green dashed line and text indicate the approximate location of the isotropic-to-cholesteric phase transition point.

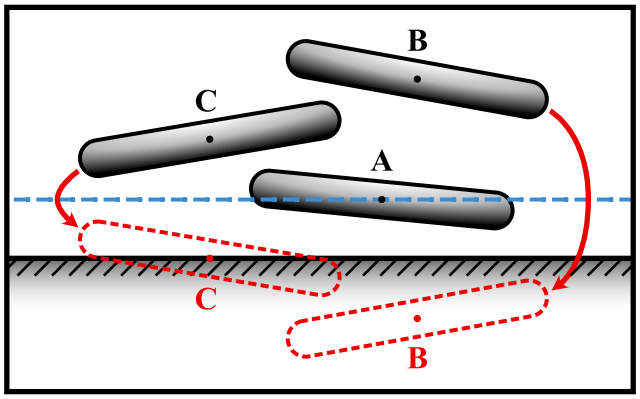

Figure 15: Diagram of three chiral spherocylinders (labelled A, B and C) in the vicinity of a chiral wall. Dashed red outlines show the mirror image reflections of molecules B and C in the mirror plane (the blue dashed line) parallel to the wall and through the centre of molecule A. When computing the interactions between molecule A and its neighbours we double the pair potential between molecules A and B but not between A and C. This is because the reflection of molecule B in the mirror plane which goes through the centre of molecule A lies entirely outside of the system beyond the lower surface. The mirror reflection of molecule C in the same mirror plane is however not entirely outside of the system and so the pair potential between A and C is not doubled.

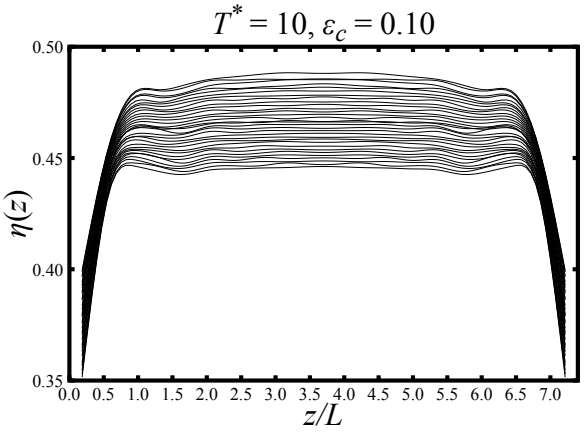

Figure 16: Same as figure 5 but for systems confined between chiral walls with the number of molecules ranging from $N = 3200$ to $N = 3600$. The temperature $T^* = 10$ and the chiral strength parameter $\epsilon_c = 0.1$.

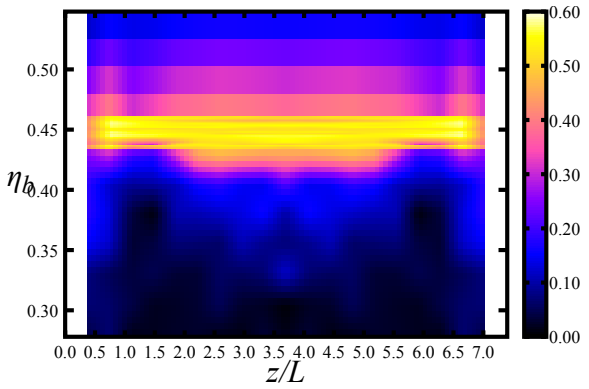

Figure 17: A contour plot of the local chiral wavenumber ($q^*(z)$), as a function of the bulk packing fraction (η_b), and distance from the lower wall (z, in units of spherocylinder length), for systems of chiral spherocylinders with an aspect ratio characterised by $L/D = 5$, and the addition of a chiral dispersion term, at a temperature of $T^* = 10$ and a chiral strength parameter $\epsilon_c = 0.1$.

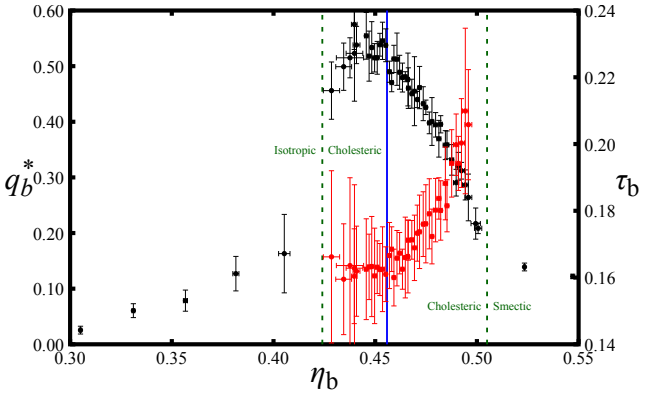

Figure 18: A plot of bulk wavenumber (q_b^*, black circles) and smectic order parameter (τ_b, red circles) versus bulk packing fraction (η_b), for systems of chiral spherocylinders with an aspect ratio characterised by $L/D = 5$ and the addition of a chiral dispersion term. The temperature $T^* = 10$ and the chiral strength parameter $\epsilon_c = 0.1$. The vertical blue line indicates the bulk packing fraction above which we see a simultaneous increase in smectic ordering and unwinding of the cholesteric helix. The green dashed lines and text indicate the approximate locations of the isotropic-to-cholesteric and cholesteric-to-smectic phase transition points.

TOC Graphic

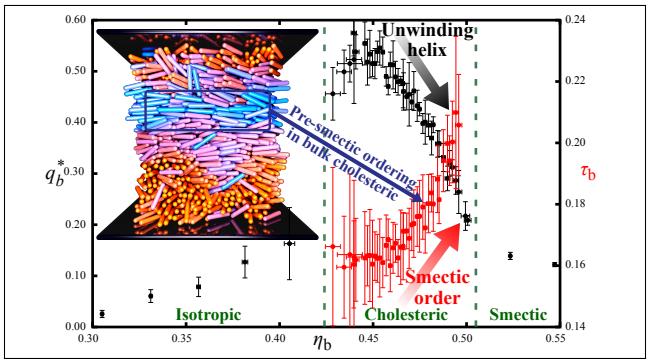
Unwinding
helix
Pre-smectic ordering
in bulk cholesteric
Smectic
order
Isotropic
Cholesteric
Smectic
q_b^*
τ_b
η_b